

---

# FREQUENCY-DEPENDENT ATTENUATION RECONSTRUCTION WITH AN ACOUSTIC REFLECTOR

---

Richard Rau<sup>†</sup>, Ozan Unal, Dieter Schweizer, Valery Vishnevskiy, Orcun Goksel

Computer-assisted Applications in Medicine, Computer Vision Lab, ETH Zurich, Switzerland.

December 8, 2021

## ABSTRACT

Attenuation of ultrasound waves varies with tissue composition, hence its estimation offers great potential for tissue characterization and diagnosis and staging of pathology. We recently proposed a method that allows to spatially reconstruct the distribution of the overall ultrasound attenuation in tissue based on computed tomography, using reflections from a passive acoustic reflector. This requires a standard ultrasound transducer operating in pulse-echo mode and a calibration protocol using water measurements, thus it can be implemented on conventional ultrasound systems with minor adaptations. Herein, we extend this method by additionally estimating and imaging the frequency-dependent nature of local ultrasound attenuation for the first time. Spatial distributions of attenuation coefficient and exponent are reconstructed, enabling an elaborate and expressive tissue-specific characterization. With simulations, we demonstrate that our proposed method yields a low reconstruction error of 0.04 dB/cm at 1 MHz for attenuation coefficient and 0.08 for the frequency exponent. With tissue-mimicking phantoms and *ex-vivo* bovine muscle samples, a high reconstruction contrast as well as reproducibility are demonstrated. Attenuation exponents of a gelatin-cellulose mixture and an *ex-vivo* bovine muscle sample were found to be, respectively, 1.4 and 0.5 on average, from images of their heterogeneous compositions. Such frequency-dependent parametrization could enable novel imaging and diagnostic techniques, as well as help attenuation compensation other ultrasound-based imaging techniques.

**Keywords** ultrasound · attenuation · speed of sound · computed tomography · limited angle tomography

## 1 Introduction

Diagnostic imaging methods aim to characterize and spatially map tissue properties in order to localize and differentiate physiological and pathological structures and processes. In addition to conventional B-mode ultrasound, which images amplitude of echos reflected locally from each tissue, there has been several techniques derived for quantifying various tissue characteristics, using acoustic interaction phenomena and novel imaging sequences: For instance, in shear-wave elastography, focused ultrasound is used to create a remote push inside tissue and the local propagation speed of the resulting shear-wave is used to estimate local shear-modulus in tissue [34, 13, 8]. For shear waves, amplitude decay over distance was measured to estimate shear-wave attenuation in [5], which was later studied for liver steatosis [3], liver transplantation [24] and under different preloading states [7]

Methods determining the propagation speed of compressional waves, i.e. speed-of-sound, relate to the tissue bulk modulus and thus have a different dependency on tissue types [16]. The estimation of speed-of-sound distributions in tissue has been studied in various setups, e.g. in transmission utilizing custom made transducer architectures [12, 22] and in pulse-echo using conventional ultrasound scanners. For the latter, the setups can be divided into two subgroups:

---

\*Funding provided by the Swiss National Science Foundation

<sup>†</sup>[rrau@ee.ethz.ch](mailto:rrau@ee.ethz.ch)

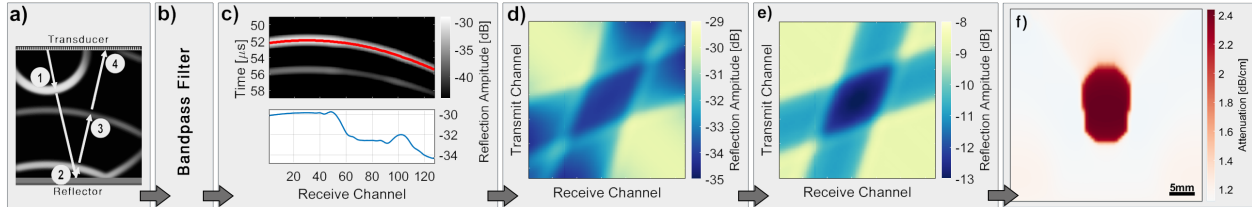


Figure 1: Processing chain for the proposed attenuation reconstruction with the reflector setup. **a)** Illustration of a wide-band wavefront progression in the medium and reflection back from the passive reflector. **b)** Band-limited filtering of the RF echo data. **c)** Echo amplitude along detected wavefront for a single transmission. Reflected amplitudes for all  $M = 128^2$  transmit/receive channel combinations **d)** before and **e)** after calibration. **f)** Reconstructed UA.

1) Based on methods that measure apparent displacements of backscattered signals insonified from different angles [32, 27, 26] and 2) based on methods that use an additional passive acoustic reflector to record corresponding time-of-flight values [30, 30]. A quantification of *in-vivo* speed-of-sound imaging was recently proposed for breast density [31] and sarcopenia assessment [29].

*Attenuation* of a compressional ultrasound (US) wave is the result of several mechanisms: First, depending on the tissue structure dimensions, US waves may *reflect* or *scatter* at interfaces of different acoustic impedances. *Viscous absorption* is caused by frictional losses. In addition, a main mode of energy loss is the result of *relaxation absorption*, which is due to consecutive wave-fronts “hitting” tissue that is locally recovering (bouncing back) from the push of an earlier wave-front [36]. These effects collectively lead to an overall *ultrasound attenuation* (UA), i.e. amplitude decay of US signals per distance they travel. Ex-vivo studies of excised tissue samples in [18, 19, 2, 1] showed that UA differs between malignant and benign lesions in breast tumors. Imaging local UA-based characteristics in tissue can be a valuable diagnostic biomarker for various clinical applications.

For imaging UA, *transmission* mode techniques that require complex, dedicated setups were proposed, e.g. a ring transducer scanning the breast immersed in a water bath. Such a method was proposed in [12], where it indicated its potential for breast tumor detection and characterization. A refinement of the method was proposed in [21] using a waveform tomography approach instead of ray based tomography, which furthermore improved the UA imaging accuracy. Such transmission mode setups are, however, not compatible with conventional clinical US systems using hand-held transducers, thus making UA imaging inaccessible for most clinical practice. To image the attenuation of compressional waves in *pulse-echo* mode is non-trivial since one cannot directly observe the propagation of waves, unlike shear-waves being observed from tissue displacements. One method to get an approximate estimate of wave amplitude decay using hand-held devices is based on power spectrum measurements of backscattered echos over certain blocks, such as in [9] and [11]. Typically a reference phantom is utilized for normalization and a (spatially weighted) regularization for reconstruction [11]. These methods indicate a potential for steatosis detection [10], however they rely on the assumption that UA attenuation in tissue is linear increasing with the frequency, which is not necessary the case [1].

A different approach to estimate the UA is to use a passive reflector in combination with a conventional US system. An early setup using such an approach for UA quantification was proposed in [20, 6], which was however not suitable for imaging (reconstructing) arbitrary spatial distributions, but only allowed quantifying values for known geometries. Furthermore, due to reconstruction instabilities, only synthetic and phantom examples could be quantified, but no actual tissue samples. Recently, we proposed a novel reconstruction approach for arbitrary spatial UA distributions in [28] based on *limited-angle computed tomography* (LA-CT) with a conventional linear-array transducer and a passive reflector. We herein analyze this method in depth and extend it to additionally characterize the local frequency-dependence of UA. This allows for our UA imaging to be applied regardless of the frequency range, as well as providing an additional novel imaging bio-marker for tissue characterization.

## 2 Methods

An overview of the proposed frequency-resolved UA reconstruction procedure is schematically depicted in Fig. 1 for a simulated example. Acoustic waves are emitted from a single transmit (Tx) channel and reflected from a plexiglas plate (density  $\rho=1180 \text{ kg/m}^3$ , speed-of-sound  $c=2700 \text{ m/s}$ ), placed at a distance  $d$  from the transducer surface. Echo signals are recorded by all receive (Rx) elements in parallel and the process is repeated for each and every Tx element, such that a full-matrix (multistatic) echo dataset is obtained. An exemplary wide-band wavefront is illustrated in Fig. 1a at different time-points: 1) after transmission, 2) while being reflected from the passive reflector plate, 3)

during echo travel, and 4) while being recorded at the transducer. The wide-band echos are then filtered to obtain band-limited signals at a defined frequency spectrum centered at frequency  $f$  (Fig. 1b). Subsequently, for each single element Tx event, the band-limited echo from the upper surface of the plexiglas reflector is delineated across the Rx channels (Fig. 1c-top) and the signal envelope amplitude along this delineated reflection is derived (Fig. 1c-bottom). The reflection amplitude readings for all Tx-Rx combinations (Fig. 1d) are then calibrated (Fig. 1e), which allows to derive the attenuation distribution in the tissue specimen by solving an inverse problem (Fig. 1f). The calibration and the reconstruction procedures are explained next.

## 2.1 Calibration of Measurements

With the assumption that the speed-of-sound and density distribution in the tissue only varies marginally, the refractive and diffractive nature of the sound waves can be neglected. This allows to assume that the band-limited ultrasound pulses at center frequency  $f$  propagate along rays with defined angles  $\theta$ . Note that transducer elements have a response as a function of direction  $\theta$ , due to destructive interference in off-axis directions, also allowing to focus energy in main beam axis. The amplitude of the reflector when transmitting with channel  $t$  and receiving with channel  $r$  is then described by

$$A_{t,r} = A_t(\theta, f) \cdot R(\theta) \cdot S_r(\theta, f) \cdot \exp\left(-\int_{\text{ray}_{t,r}} \alpha(x, y, f) dl\right), \quad (1)$$

where  $R(\theta)$  is the incident-angle dependent reflection coefficient at the reflector interface, and  $A_t(\theta, f)$  and  $S_r(\theta, f)$  are, respectively, the band-limited amplitude of Tx element  $t$  and the sensitivity of Rx element  $r$ , at center frequency  $f$  and transducer directivity  $\theta$ . The exponent describes frequency-dependent amplitude decay based on the line integral of attenuation  $\alpha$  along ray $_{t,r}$  from element  $t$  to  $r$ .

To derive the attenuation from  $A_{t,r}$ , any confounding factors in (1) must first be compensated for, such as transducer impulse-response influence in both  $A_t(\theta, f)$  and  $S_r(\theta, f)$  as well as reflection characteristics in  $R(\theta)$ . Considering the impulse response, the band-limited signals are normalized with a calibration experiment in water, where the speed-of-sound  $c_{\text{water}}$  and the attenuation coefficient  $\alpha_{\text{water}}$  are known from the literature, given the water temperature and imaging frequency. By using predetermined frequency bandwidths and reflector distances in the water calibration the same as in the subsequent tissue experiments,  $A_t(\theta, f)$  and  $S_r(\theta, f)$  components can be effectively estimated and factored out. However,  $R(\theta)$  is still likely to differ, because of the speed-of-sound mismatch in water and tissue. Such reflection coefficient changes at the acoustic reflector interface can nevertheless be analytically estimated using Snell's law, as the wavelength ( $\approx 300 \mu\text{m}$ ) is small compared to the reflector dimensions. One can then write the reflection coefficient at the interface of the reflector and some medium  $k=\{\text{water,tissue}\}$  as follows:

$$R_k(\theta) = \frac{m_k \cos(\theta) - n_k \sqrt{1 - \frac{\sin^2(\theta)}{n_k^2}}}{m_k \cos(\theta) + n_k \sqrt{1 - \frac{\sin^2(\theta)}{n_k^2}}}, \quad (2)$$

where speed-of-sound ratio  $n_k=c_{\text{reflector}}/c_k$  and density ratio  $m_k=\rho_{\text{reflector}}/\rho_k$ . We herein assume  $\rho_{\text{tissue}} \approx \rho_{\text{water}} \approx 1000 \text{ kg/m}^3$  and that the speed-of-sound is dispersion-free (i.e., no frequency dependence) within the range of the utilized imaging frequency bandwidth. A normalized reflection amplitude matrix  $B'$  shown in Fig. 1e can then be computed with its elements corresponding to Tx  $t$  and Rx  $r$  being

$$b'_{t,r} = \frac{A_{t,r,\text{tissue}} R_{\text{water}}(\theta)}{A_{t,r,\text{water}} R_{\text{tissue}}(\theta)}. \quad (3)$$

With this together with (1), we can relate the calibrated and band-limited measurements at frequency  $f$  to attenuation  $\alpha(x, y, f)$  at image location  $(x, y)$  by

$$b_{t,r} = \ln b'_{t,r} = - \int_{\text{ray}_{t,r}} \alpha(x, y, f) dl \approx - \sum_{i \in \text{ray}_{t,r}} l_i \alpha_i(f), \quad (4)$$

where the ray integral is discretized as a summation over a reconstruction grid. For this discretization, we use local attenuation value  $\alpha(x, y)$  weighted by its path length within the grid element  $(x, y)$ .

## 2.2 Image Reconstruction of Attenuation

Given  $M$  logarithms of normalized reflection amplitudes  $\mathbf{b} \in \mathbb{R}^M$  at a specified frequency band, we perform a tomographic reconstruction of the spatial UA distribution on a  $N_1 \times N_2$  spatial grid by formulating the following convex optimization problem:

$$\hat{\alpha}(f) = \arg \min_{\alpha(f)} \|\mathbf{L}\alpha(f) + \mathbf{b}(f)\|_1 + \lambda \|\mathbf{D}\alpha(f)\|_1, \quad (5)$$

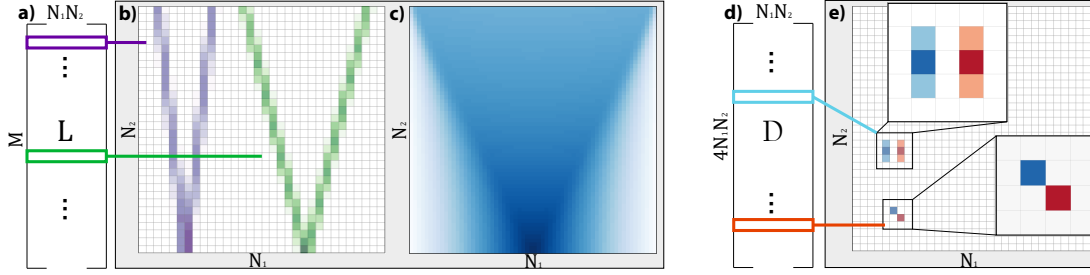


Figure 2: Reconstruction matrix  $\mathbf{L}$  (a) with two representative paths depicted (b). The path distribution (c) illustrates the spatial coverage of tomographic projections in the imaging field of view. Regularization matrix  $\mathbf{D}$  (d) with a horizontal Sobel and a diagonal Roberts kernel (e), where blue and red indicate positive and negative components with zero-sum.

where  $\mathbf{L} \in \mathbb{R}^{M \times N_1 N_2}$  is the sparse ray path matrix (cf. Fig. 2) that implements (4) and  $\alpha(f) \in \mathbb{R}^{N_1 N_2}$  is the reconstructed image at the center frequency  $f$ , which is defined by the earlier band-pass filtering (cf. Fig. 1b). Due to the ill-conditioning of  $\mathbf{L}$ , a regularization term controlled by weight  $\lambda$  encourages spatial smoothness. Similarly to [26, 27, 30, 33], we herein use  $\ell_1$ -norm for both the data and regularization terms for robustness to outliers in, respectively, the measurements and the reconstructed image (edges) [15]. Due to a lack of full angular coverage of measurements, regularization matrix  $\mathbf{D}$  implements LA-CT specific image filtering to suppress streaking artifacts orthogonal to missing projections via anisotropic weighting of directional gradients [30]. In axis-aligned directions a Sobel kernel, and in diagonal directions a Roberts kernel is used [27] (see Fig. 2d/e). Similarly to [32], we herein utilize a  $\kappa=0.9$  anisotropic weighting to regularize stronger in lateral direction, taking into account the uneven distribution of measurement paths. In this paper we empirically set  $\lambda=0.6$  for all experiments. For the numerical solution of the optimization problem (5), a limited-memory BroydenFletcherGoldfarbShanno (L-BFGS) algorithm [4, 14, 17, 35] from the unconstrained optimization package `minFunc`<sup>3</sup> is implemented.

### 2.3 Frequency-Dependent Attenuation Reconstruction

To characterise the frequency-dependent nature of attenuation, wide-band RF echo signals are first band-pass filtered prior to reconstruction. In this work, for analyzing the echos acquired at an imaging center frequency of 5 MHz, we used 1 MHz-bands at nominal center frequencies at [3.5, 4.5, ..., 8.5] MHz. Band-pass filtering is herein implemented using the MATLAB 2019a function `bandpass`, which implements a minimum-order filter with a stop-band attenuation of 60 dB. The processing is illustrated for a simulated dataset in Fig. 3a, in which UA reconstructions at three different frequency bands [8.1, 6.1, 3.9] MHz are depicted. The true center frequency indicated in the northwest corner of each reconstruction are slightly offset to the nominal values [8.5, 6.5, 3.5] MHz, because the reported *true* center frequencies are evaluated after filtering as the spectral weighted average of the bandpass filtered signal. Since the emitted wide-band pulse is approximately Gaussian with a peak at 5 Mhz, the weighted averages  $f$  are shifted towards 5 Mhz. In Fig. 3b, the frequency-dependent attenuation values are shown for two regions, within the inclusion and outside. These plots already yield a spectral fingerprint of the attenuation characteristics in each tissue. To parametrize such spectroscopic attenuation reconstructions in a standardized way, one can assume the conventional power-law relation:

$$\alpha(f) = \alpha_0 f^y, \quad (6)$$

where attenuation is a function of frequency with medium-specific attenuation coefficient  $\alpha_0$  and medium-specific exponent  $y$ . Accordingly, separately at each spatial image location,  $\alpha_0$  and  $y$  are estimated by least-squares fitting of the power-law function across the band-limited reconstructions as shown in Fig. 3c and d.

Note that the attenuation term in (5) could have alternatively been replaced by the power-law equation (6), for solving all frequency bandwidths simultaneously. This could provide robustness by regularizing reconstructions across frequencies by their expected power-law relation as well as allowing for the direct spatial regularization of the two final parameters. However, this would also increase the optimization problem size in several folds, impeding an efficient numerical solution.

<sup>3</sup><https://www.cs.ubc.ca/~schmidtm/Software/minFunc.html>

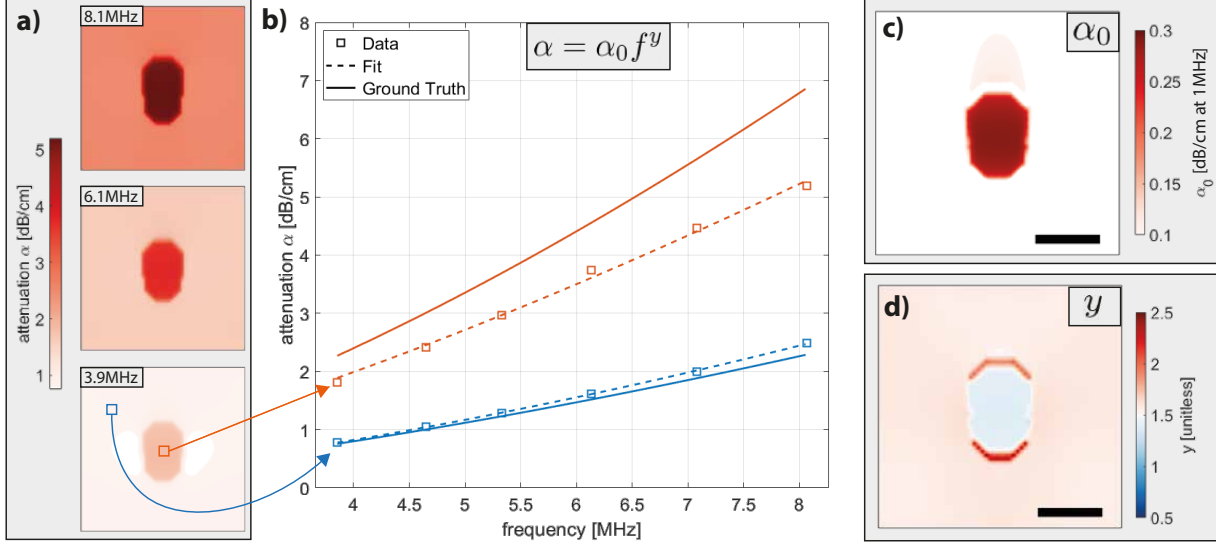


Figure 3: **a)** Attenuation reconstructions within individual frequency bands. **b)** Frequency-dependent attenuation characterized at two locations (orange) in and (blue) outside the inclusion. By fitting the power-law at each pixel, the corresponding maps for attenuation coefficient  $\alpha_0$  (c) and the frequency exponent  $y$  (d). The scale-bars represent 10 mm.

### 3 Experiments

**Metrics.** We used the following metrics for a quantitative analysis of the simulation results:

- Root-mean-squared-error:  

$$\text{RMSE} = \sqrt{\|\hat{\mathbf{x}} - \mathbf{x}^*\|_2^2 / N},$$
where  $\mathbf{x}$  represents maps of  $\alpha$ ,  $\alpha_0$ , or  $y$ , and  $N$  is the number of map pixels. The  $*$  and  $\hat{\phantom{x}}$  indicate, respectively, the ground-truth and our reconstruction.
- Contrast-ratio fraction:  

$$\text{CRF} = \hat{C} / C^*,$$
where  $C = 2 \frac{|\mu_{\text{inc}} - \mu_{\text{bkg}}|}{|\mu_{\text{inc}}| + |\mu_{\text{bkg}}|}$  with mean inclusion and background values  $\mu_{\text{inc}}$  and  $\mu_{\text{bkg}}$ , respectively, where the inclusion is delineated from the ground-truth map.
- Contrast-to-noise ratio:  

$$\text{CNR} = |\mu_{\text{inc}} - \mu_{\text{bkg}}| / \sqrt{\sigma_{\text{inc}}^2 + \sigma_{\text{bkg}}^2},$$
where  $\sigma^2$  represents the variance.

**Simulation Study.** To evaluate the accuracy of frequency-dependent UA reconstructions, three simulations with different UA patterns were performed as shown in Fig.4. The patterns were selected herein to assess inclusions along and orthogonal to the tomographic projections as well as with positive and negative variation with respect to the background. Acoustic propagation and received echo signals were simulated using k-Wave ultrasound simulation toolbox [37] using a spatial grid resolution of  $37.5 \mu\text{m}$ . The inclusions are simulated with a spatial variation in attenuation constant  $\alpha_0(x, y)$ . As this toolbox does not allow to spatially vary the power-law dependence parameter  $y$ , it is kept constant at  $y = 1.5$  for this numerical evaluation. Full-matrix acquisition was simulated at a center frequency of 5 MHz with pulses of 5 cycles. The transducer was simulated as a 128 channel array (i.e.  $M = 128^2$ ) with a pitch of  $300 \mu\text{m}$ .

**Phantom and *Ex-vivo* Tissue Study.** A tissue-mimicking gelatin phantom was prepared with 10% gelatin in water per weight. We created non-scattering and scattering phantoms; for the latter, using 1% per-weight Sigmacell Cellulose Type 50 (Sigma Aldrich, St. Louis, MO, USA). Fresh bovine skeletal muscle was used as *ex-vivo* tissue samples. Using combinations of the above, we created four phantoms:

- Phantom #1: A single *ex-vivo* muscle inclusion in scattering gelatin background

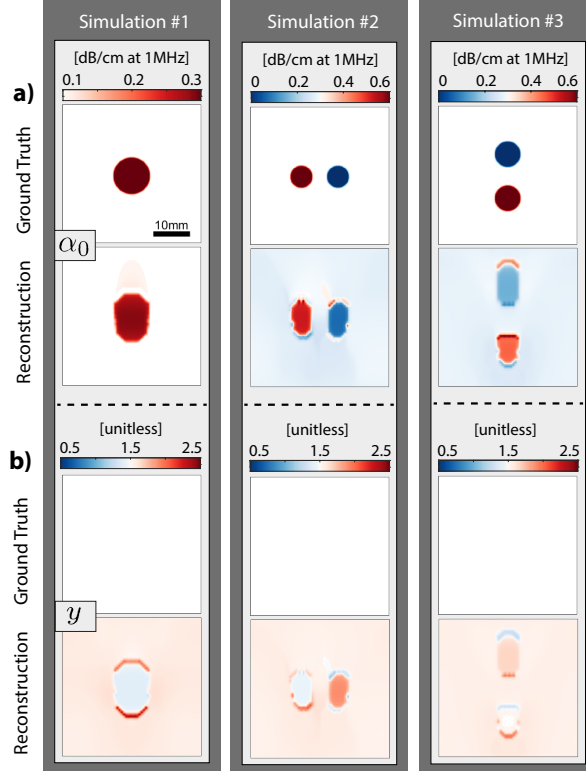


Figure 4: Frequency-dependent UA image reconstruction for three simulations. Each column shows one simulation with the  $\alpha_0$ -maps (a) and the  $y$ -maps (b). Above each reconstruction map, the ground truth maps are shown.

- Phantom #2: A single *ex-vivo* muscle inclusion in non-scattering gelatin background
- Phantom #3: A single scattering gelatin inclusion in *ex-vivo* muscle background
- Phantom #4: Two non-scattering gelatin inclusions in *ex-vivo* muscle background

Experiments were performed with the samples submerged in distilled water at room temperature. Muscle samples were imaged with the fibers oriented orthogonal to the imaging plane, to prevent potential confounding effects from anisotropic acoustic propagation along tissue fibers, as this is currently not accounted for in our model. Data acquisition was performed with a Verasonics Vantage 128-channel system connected to a Philips ATL L7-4 transducer (Verasonics, Kirkland, WA, USA). Analogous to the simulation setup, we used a Tx center frequency of 5 MHz and a pulse length of 5 cycles. The reflector distance varied from 30 mm to 46 mm depending on the sample size. For normalization of the *ex-vivo*/phantom amplitude matrices at a given reflector depth  $d$ , we acquired calibration measurements a-priori in distilled water at room temperature at multiple reflector depths [31,35,...,47] mm. For a given phantom measurement, we then computed the desired calibration values  $b_{t,r}$  at  $d$  via linear interpolation from the closest two calibration acquisitions.

## 4 Results and Discussion

### 4.1 Simulation Experiments

Three simulations (#1–#3) shown in Fig. 4 were conducted as representative cases with inclusions separated laterally and axially as well as with both positive and negative contrast to background. Simulation #1 is the case illustrated earlier in Fig. 3. Given the ground truth maps in Fig. 4 it can be seen that the attenuation coefficient  $\alpha_0$  contrast is successfully reconstructed. The frequency exponent  $y$ -maps should not present any contrast, since the k-Wave simulated ground-truth data does not allow to spatially vary  $y$ . Reconstructed  $y$ -maps are seen to exhibit a deviation from such constant ground-truth value, with a fixed background offset and some artifacts along the axial edges of inclusions. These artifacts originate from the unconstrained reconstructions at different frequency bands, which yields artificial elongation of inclusions through regularization, i.e. the higher the frequency band, the longer an inclusion is

Table 1: Quantitative evaluation of frequency-dependent UA reconstructions in simulations.

	$\alpha_0$	$y$
RMSE	$(0.04 \pm 0.02)$ dB/cm at 1 MHz	$0.08 \pm 0.02$
CNR	$(0.4 \pm 0.2)$	-
CRF	$(71 \pm 28)$ %	-

Table 2: Comparison of the attenuation imaging using frequency dependent estimation or fullband frequency averaging.

	$\alpha_0 f^y$	Fullband
RMSE	$(0.4 \pm 0.1)$ dB/cm	$(0.5 \pm 0.2)$ dB/cm
CNR	$(4.2 \pm 2.3)$	$(2.4 \pm 1.9)$
CRF	$(53 \pm 23)$ %	$(38 \pm 29)$ %

axially. This effect can be observed in Fig. 3a, where the inclusion shape at 8.1 MHz is axially longer compared to that at 3.9 MHz. This then results in artifactually higher UA values outside the axial edges at higher frequencies, thus resulting in increased  $y$  values. Such axial elongation of inclusions is a known limitation of LA-CT imaging due to missing lateral projections, as also reported and discussed in [28, 30].

In Fig. 4, it is observed that with increasing UA distribution complexity (i.e., from simulation #1 to #3), the reconstruction accuracy decreases. In particular, axially-separated inclusions are reconstructed poorer compared to those laterally separated. This is due to the transmit-receive paths traversing the tissue in a mostly axial direction and hence lateral projections being missing in the resulting LA-CT. In general, within the inclusions a shift of  $\alpha_0$  towards background values is observed (cf. Fig. 4). This is due to the lack of lateral projections combined with the regularization term in (5) axially elongating the inclusions and thus spreading the UA values over a larger area. Since their cumulative effect shall stay the same, their per-pixel values are thus effectively averaged with the background, inversely proportional to such artifactual area increase.

To quantify the performance of the frequency-dependent UA reconstructions, we evaluate RMSE, CNR and CRF for each simulation and report in Tab.1 the corresponding average values and standard deviations over all three simulations. We evaluate the accuracy of image reconstruction using RMSE. RMSE of  $\alpha_0$  is  $(0.04 \pm 0.02)$  dB/cm at 1 MHz. As  $\alpha_0$  values reach up to 0.6 dB/cm at 1 MHz, this demonstrates that an accurate characterization of the attenuation coefficient is possible. With an average RMSE of  $0.08 \pm 0.02$  for  $y$ , the relative estimation error with respect to the prescribed  $y = 1.5$  is below 6%, indicating a relatively good estimation of frequency exponent. The contrast metrics (CNR and CRF) for  $\alpha_0$  demonstrate that the inclusions can be successfully distinguished by  $\alpha_0$  reconstructions, at a contrast similar to their prescribed ground-truth value. Note that the contrast metrics are only computed for  $\alpha_0$ , since no contrast could be defined for  $y$  in simulations.

To estimate how frequency-dependent UA imaging compares to the frequency-averaged fullband UA reconstructions [28], we compute the overall attenuation  $\alpha$ -maps using  $\alpha = \alpha_0 f^y$  for each pixel at the known transmit center frequency of 5 MHz (Fig. 5a). The corresponding fullband reconstructions are shown in Fig. 5b along with the ground-truth images derived at 5 MHz from  $\alpha_0$ - and  $y$ -maps prescribed the corresponding simulations in Fig. 5c. It is seen that estimating  $\alpha_0$  and  $y$  prior to deriving the overall attenuation improves UA characterization significantly. This observation is corroborated by RMSE, CNR, and CRF metrics averaged over simulations for both methods as reported in Tab.2. On average, the UA estimation accuracy (RMSE) improves by 20% along with a substantial enhancement in contrast, which is reflected by the higher CNR (75% improvement) and CRF (40% improvement). In an actual imaging scenario such higher contrast would enable easier abnormality identification and characterization, especially in the challenging cases where more heterogeneous compositions are images (as in simulations #2 and #3). In addition to the improved contrast, the frequency-dependent UA imaging allows to characterize tissue with two biomarkers, potentially expressive for different diagnostic or pathological effects, independently or in combination.

## 4.2 Ex-vivo Experiments

The results of the gelatin phantom and ex-vivo experiments are shown in Fig.6 with their corresponding B-Mode images and attenuation reconstructions for the frequency-dependent ( $\alpha_0, y$ ) as well as the fullband frequency-averaged ( $\alpha$ ) attenuation parameters. For the frequency-resolved approach, an equivalent  $\alpha$  is also computed for comparison from the reconstructed coefficient and exponent maps based on (6). For the phantoms #1 & #2 with muscle inclusions in gelatin, a clear contrast is visible for all UA reconstructions (Fig.6c-f). With our proposed frequency-dependent method, it can be seen that the observed attenuation contrast originates from a variation not only in attenuation co-

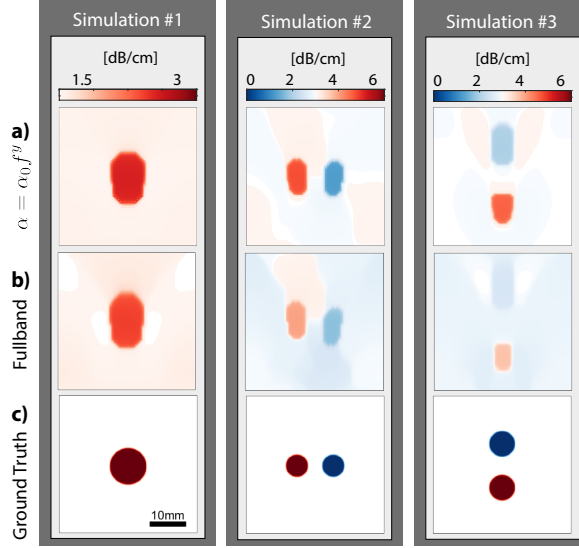


Figure 5: Comparison of frequency-dependent and fullband UA imaging. The columns represent different simulations with the attenuation images derived (a) by the frequency-dependent estimations using (6) and (b) by the fullband as in [28]. Ground-truth attenuation maps in (c) are derived using the ground truth  $\alpha_0$  and  $y$  given the transmit center frequency.

efficient but also in frequency-dependence. For phantom #3, the reconstructed values with our proposed frequency-resolved method are consistent with phantoms #1 and #2, where the inclusion and background are inverted. Compared to the fullband method,  $\alpha_0$ - and  $y$ -maps are seen to better preserve inclusion geometry with a reduced axial elongation, corroborating the earlier findings in the simulations. This shape accuracy is especially important in cases, where the inclusions are not directly observable in the B-Mode images, e.g. in phantom #3 where the scattering gelatin and the surrounding muscle may be isoechoic.

To suppress axial edge artifacts, especially in  $y$ -maps, a possible solution would be to first delineate target regions for UA characterization and then to solve the reconstruction problem with UA constrained as piece-wise constant within each such predefined region. Such regions could be delineated manually or automatically from B-Mode images or from  $\alpha_0$ -maps of initial unconstrained UA reconstructions.

In general, the background reconstructions deteriorate towards the two lower corners, likely due to few to no rays in these regions, as also illustrated in Fig. 2c. These errors may then affect the rest of the image, also deteriorating how well the inclusions, especially those nearby these corners, are reconstructed. Consequently, phantom #4 with two inclusions on the sides exhibits a poor reconstruction. Indeed, in contrast to the superior performance of the frequency-resolved method for phantoms #1–#3, for phantom #4 it yields poorer results compared to the fullband, with large localization and geometry estimation errors. Surprisingly, the two inclusions with the same material are not even characterized similarly in the reconstructions for neither  $\alpha_0$  nor  $y$ . Nevertheless, with the frequency-dependent  $\alpha_0$ - and  $y$ -maps and using (6), an attenuation map  $\alpha$  (Fig.6e), which is very similar to the fullband approach, can be derived. This then recovers any lost contrast, even for phantom #4, where  $\alpha_0$  and  $y$  reconstructions are suboptimal. This observation is supported quantitatively by average CNR of attenuation across *ex-vivo* samples being comparable as  $(3.3 \pm 2.6)$  for the fullband method and  $(3.1 \pm 2.2)$  using (6) from frequency-resolved parameter maps. These results also demonstrate that our fullband as well as frequency-resolved methods are applicable to actual tissue acquisitions.

To quantify reproducibility of our attenuation imaging and characterization for the same material in different configurations, we conducted the following study on the *ex-vivo* dataset. In total three materials were used in phantoms #1–#4: bovine muscle tissue, pure gelatin, and gelatin-cellulose mixture. It is expected and desired that the same material is reconstructed as the same value across different phantoms. To quantify such consistency and constancy, in Fig.7 we compare the distributions of reconstructions within manually-delineated material regions depicted in Fig.6. We present such distributions along with the median values (red lines in Fig.7) for frequency-dependent  $\alpha_0$  and  $y$  reconstructions as well as fullband  $\alpha$  reconstructions. In these comparisons,  $\alpha$  derivations using (6) is omitted, since it closely follows fullband  $\alpha$  distributions, as demonstrated earlier in Fig.6. To quantify constancy across the phantoms, we compare the median values, where their statistical distribution (mean and standard-deviation) for the same material across phantoms is reported in Table 3. For the scattering gelatin with cellulose (referred as *gelatin+*), a low standard-deviation



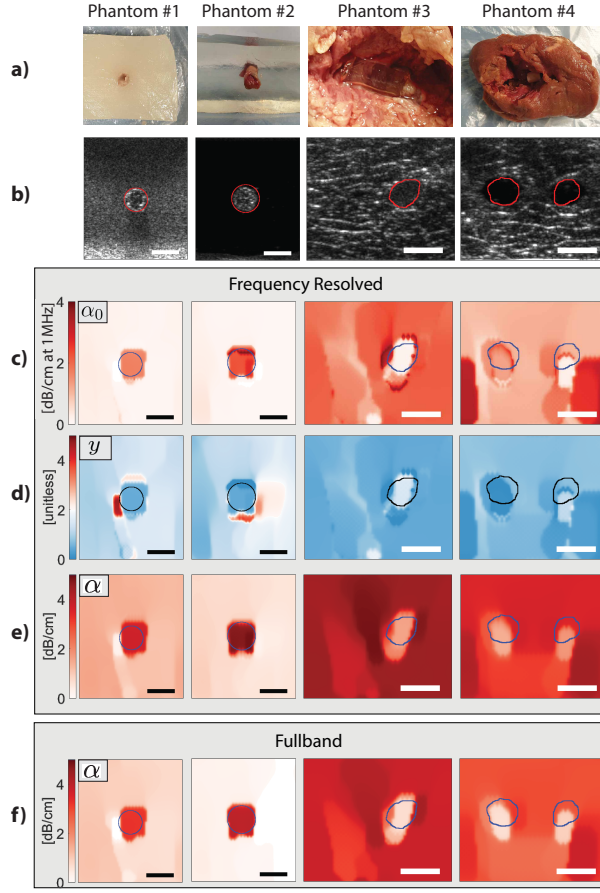


Figure 6: Reconstructions from gelatin phantoms and *ex-vivo* bovine muscle. **a)** Sample pictures for: muscle inclusions in gelatin (#1) with and (#2) without cellulose; and muscle samples with gelatin inclusions (#3) with and (#4) without cellulose. **b)** Corresponding B-Mode images. Reconstructions of **d)** attenuation coefficient  $\alpha_0$  and **e)** exponent  $\gamma$  using the proposed frequency-resolved method. **f)** Frequency-averaged reconstructions using the fullband spectrum [28]. The scale-bars represent 10 mm.

Table 3: Reproducibility of material characterization over different phantoms for the two methods.

	$\alpha$ (Fullband)
Muscle Tissue	$(3.41 \pm 0.49)$ dB/cm
Gelatin+	$(0.79 \pm 0.04)$ dB/cm
Gelatin	$(1.13 \pm 1.40)$ dB/cm
	$\alpha_0 f^\gamma$ (Frequency Resolved)
Muscle Tissue	$(1.86 \pm 0.51)$ dB/(MHz $^{(0.49 \pm 0.11)}$ cm)
Gelatin+	$(0.15 \pm 0.00)$ dB/(MHz $^{(1.36 \pm 0.12)}$ cm)
Gelatin	$(0.71 \pm 0.88)$ dB/(MHz $^{(0.83 \pm 0.51)}$ cm)

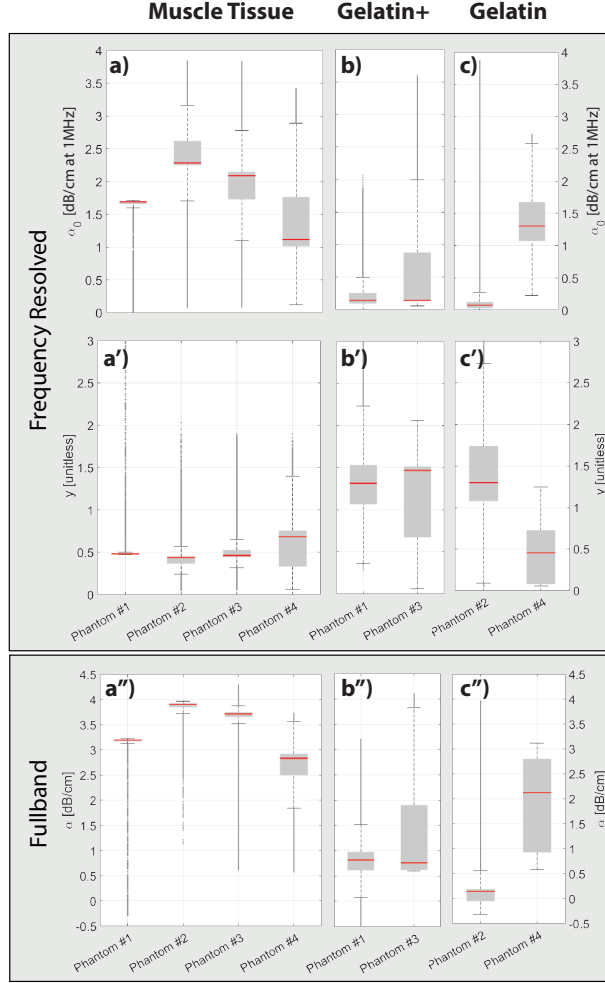


Figure 7: Distributions of attenuation values for difference materials: muscle tissue (a), gelatin with cellulose (b), and pure gelatin (c). Frequency-dependent parameters  $\alpha_0$  and  $y$  are shown, respectively, in (a-c) and (a'-c'). Fullband frequency-averaged attenuation is shown in (a''-c'').

in Table 3 indicates a high reproducibility considering all three UA parameters (also can be observed in Fig.7b/b'/b''). Despite an expected natural tissue heterogeneity, all reconstructions of the muscular tissue also follow relatively tight distributions with somewhat similar values as seen in Figs.7a/a'/a''. Muscle tissue appears to have a high  $\alpha$  and  $\alpha_0$  whereas a low exponent  $y$ , and accordingly presents a stark contrast to gelatin+. For the pure gelatin case, we expect an overall attenuation lower than gelatin+ due the lack of scattering that contributes to attenuation. Indeed, for phantom #2 compared to #1 & #3, both  $\alpha_0$  and  $\alpha$  are significantly lower, as expected, cf. Fig.7b/b''/c/c''. Interestingly,  $y$  is similar with and without scattering, cf. (Fig.7b'/c'). This can be explained by the fact that frequency-dependent attenuation components are mostly relaxation and viscous absorption, and not scattering. Also the cellulose scatterers of size  $50 \mu\text{m}$  are smaller than the wavelength of the highest frequency band, thus interacting with all involved frequency bands similarly as a scattering source. Such observations unfortunately cannot be made from phantom #4, the reconstructions of which as mentioned above were affected severely by artifacts.

### 4.3 Extrapolation of Attenuation Characteristics

With the characterization of the power-law coefficients of frequency-dependent attenuation, the observations can now be extrapolated to a wider hypothetical frequency range using (6), as presented in Fig. 8 for the muscle tissue and the gelatin+ material using the average values from Tab. 3. We can then conclude that under 20 MHz the contrast between the attenuation values  $\alpha$  of these two materials would be maximized at 5.6 MHz as  $\Delta\alpha = 2.8 \text{ dB/cm}$ . Conversely, at  $\approx 18 \text{ MHz}$  as seen in Fig. 8, the two materials will not exhibit any contrast at all, i.e.  $\Delta\alpha = 0$ . This demonstrates that

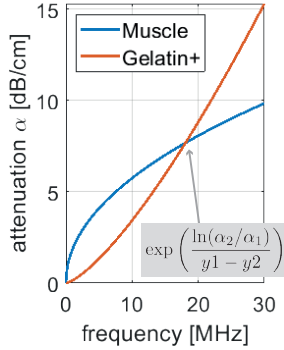


Figure 8: Extrapolated attenuation of the muscle and gelatin+ materials. At  $\approx 18$  MHz, calculated as shown in the figure, no discrimination would theoretically be possible between the two materials.

using a frequency-averaged UA imaging, the achieved contrast may highly depend on the imaging frequency. Using an inappropriate imaging frequency in a practical scenario may potentially lead to misclassification of a tumor or failing to detect it entirely. Our proposed frequency resolved attenuation imaging method redeems this limitation of having to select an optimal imaging frequency, which likely unknown *a-priori* and can provide a characterization independent of frequency range and thus imaging transducer and depth selection.

#### 4.4 Further Discussion

Herein we only take the speed-of-sound difference between water calibration and target tissue into account for compensating for the reflection coefficient differences, cf. (3). Tissue speed-of-sound difference from the water calibration may, however, additionally affect the angular beam profile of the transducer elements, hence confounding the assumption of amplitude matrix constancy between water and tissue in (3). Nevertheless, we believe such discrepancy of the beam profiles to be minimal, given the successful reconstruction results with both our frequency-resolved and fullband attenuation imaging methods.

In the experiments above we utilized a transmit pulse of five cycles. This could be shortened for the full spectral bandwidth of the transmit pulse to be extended up to the full transducer bandwidth, hence allowing for a wider range of reconstruction frequencies (cf. Fig 1b).

Similarly to most earlier works in US-CT, we herein assume a straight ray propagation, which is however only true for homogeneous speed-of-sound distributions. Local speed-of-sound inhomogeneities may indeed refract and aberrate wavefronts, resulting in inaccurate amplitude readings as well as the assumed wavepaths (e.g. Fig.2b) being different than actual wavepaths – both leading to inaccuracies in reconstruction. A potential remedy would be to correct ray refractions based on speed-of-sound reconstructions, e.g. derived using time-of-flight measurements [33].

For a multi-parametric tissue characterization, our proposed method can add two additional imaging bio-markers complementary to robust speed-of-sound imaging methods [27, 26], which may be superior to elastography [16].

in addition to using the proposed attenuation imaging for diagnostic purposes, the derive UA distribution can also be utilized to improve other ultrasound imaging modalities. Similarly to [26], where speed-of-sound imaging is used to correct for aberration effects in beamforming, the UA estimations can be used to locally compensate the gain, thus e.g. homogenizing the B-mode image appearance, improving displacement estimations in shear wave imaging or enhancing optoacoustic [23] and functional imaging [25].

A practical limitation of the herein proposed frequency-resolved attenuation imaging is the computational time required for the reconstructions due to the iterative numerical optimization employed. A deep variational network solution such as in [38, 39] with reconstruction times in the range of milliseconds potentially allows overcoming this restriction towards real-time imaging.

## 5 Conclusions

In this paper we have presented a novel approach for reconstructing frequency-dependent ultrasound attenuation distribution in tissue, which allows to locally characterize tissue with two biomarkers – namely the attenuation coefficient and frequency exponent. This method allows for a more accurate reconstruction of UA distribution compared to our earlier method in [28] using fullband frequency-averaged reconstruction of a single attenuation parameter. Our experiments with numerical simulations, tissue-mimicking gelatin phantoms, and *ex-vivo* indicate a high overall reconstruction accuracy with a mean RMSE of simulated phantoms as 0.04 dB/cm at 1 MHz for attenuation coefficient

$\alpha_0$  and 0.08 for frequency exponent  $y$  Compared to fullband reconstructions, the frequency-dependent method offers an almost two-fold improvement in CNR as in Table 2. Requiring only a minimal hardware add-on as a passive acoustic reflector, the proposed imaging is readily translatable to clinical applications where the opposite side of the imaged tissue region is accessible, e.g. imaging the breast, the extremities, and male genitalia.

## References

- [1] Bamber, J.C., Hill, C.R., . Acoustic properties of normal and cancerous human liver. dependence on pathological condition. *Ultrasound in Medicine & Biology* 7, 121–133.
- [2] Bamber, J.C., Hill, C.R., 1979. Ultrasonic attenuation and propagation speed in mammalian tissues as a function of temperature. *Ultras Med Biol* 5, 149–157.
- [3] Barry, C.T., Mills, B., Hah, Z., Mooney, R.A., Ryan, C.K., Rubens, D.J., Parker, K.J., . Shear wave dispersion measures liver steatosis. *Ultrasound in Medicine & Biology* 38, 175–182.
- [4] Broyden, C.G., 1970. The Convergence of a Class of Double-rank Minimization Algorithms 1. General Considerations. *IMA Journal of Applied Mathematics* 6, 76–90.
- [5] Catheline, S., Gennisson, J.L., Delon, G., Fink, M., Sinkus, R., Abouelkaram, S., Culioli, J., 2004. Measurement of viscoelastic properties of homogeneous soft solid using transient elastography: An inverse problem approach. *The Journal of the Acoustical Society of America* 116, 3734–3741.
- [6] Chang, C.H., Huang, S.W., Yang, H.C., Chou, Y.H., Li, P.C., 2007. Reconstruction of ultrasonic sound velocity and attenuation coefficient using linear arrays: Clinical assessment. *Ultras Med Biol* 33, 1681–1687.
- [7] Chintada, B.R., Rau, R., Goksel, O., . Nonlinear characterization of tissue viscoelasticity with acoustoelastic attenuation of shear-waves. *arXiv:2002.12908* .
- [8] Chintada, B.R., Rau, R., Goksel, O., 2019. Acoustoelasticity analysis of shear waves for nonlinear biomechanical characterization of oil-gelatin phantoms, in: 2019 IEEE International Ultrasonics Symposium (IUS), pp. 423–426.
- [9] Coila, A.L., Lavarello, R., . Regularized spectral log difference technique for ultrasonic attenuation imaging. *IEEE Trans. Ultrason., Ferroelect., Freq. Contr.* 65, 378–389.
- [10] Deeba, F., Ma, M., Pesteie, M., Terry, J., Pugash, D., Hutcheon, J.A., Mayer, C., Salcudean, S., Rohling, R., 2019a. Attenuation coefficient estimation of normal placentas. *Ultrasound in Medicine & Biology* 45, 1081–1093.
- [11] Deeba, F., Schneider, C., Mohammed, S., Honarvar, M., Tam, E., Salcudean, S., Rohling, R., 2019b. SWTV-ACE: Spatially weighted regularization based attenuation coefficient estimation method for hepatic steatosis detection, in: *Medical Image Computing and Computer Assisted Intervention MICCAI 2019*, pp. 610–618.
- [12] Duric, N., Littrup, P., Poulou, L., Babkin, A., Pevzner, R., Holsapple, E., Rama, O., Glide, C., 2007. Detection of breast cancer with ultrasound tomography: First results with the Computed Ultrasound Risk Evaluation (CURE) prototype. *Medical Physics* 34, 773–785.
- [13] Eby, S.F., Song, P., Chen, S., Chen, Q., Greenleaf, J.F., An, K.N., 2013. Validation of shear wave elastography in skeletal muscle. *J Biomech* 46, 2381–2387.
- [14] Fletcher, R., 1970. A new approach to variable metric algorithms. *The Computer Journal* 13, 317–322.
- [15] Fu, H., Ng, M.K., Nikolova, M., Barlow, J.L., . Efficient minimization methods of mixed l2-l1 and l1-l1 norms for image restoration. *SIAM J. Sci. Comput.* 27, 1881–1902.
- [16] Glozman, T., Azhari, H., 2010. A method for characterization of tissue elastic properties combining ultrasonic computed tomography with elastography. *Journal of Ultrasound in Medicine* 29, 387–398.
- [17] Goldfarb, D., 1970. A family of variable-metric methods derived by variational means. *Mathematics of Computation* 24, 23–23.
- [18] Goss, S.A., Johnston, R.L., Dunn, F., 1978. Comprehensive compilation of empirical ultrasonic properties of mammalian tissues. *J Acoust Soc Am* 64, 423–457.
- [19] Goss, S.A., Johnston, R.L., Dunn, F., 1980. Compilation of empirical ultrasonic properties of mammalian tissues. II. *J Acoust Soc Am* 68, 93–108.
- [20] Huang, S.W., Li, P.C., 2005. Ultrasonic computed tomography reconstruction of the attenuation coefficient using a linear array. *IEEE Trans Ultrason Ferr Freq Control* 52, 2011–2022.

- [21] Li, C., Sandhu, G.Y., Boone, M., Duric, N., 2017. Breast imaging using waveform attenuation tomography, in: *Procs SPIE Med Imaging*, p. 101390A.
- [22] Malik, B., Terry, R., Wiskin, J., Lenox, M., . Quantitative transmission ultrasound tomography: Imaging and performance characteristics. *Medical Physics* 45, 3063–3075.
- [23] Mercep, E., Herraiz, J.L., Dean-Ben, X.L., Razansky, D., . Transmission-reflection optoacoustic ultrasound (TROPUS) computed tomography of small animals. *Light: Science & Applications* 8, 18.
- [24] Nenadic, I.Z., Urban, M.W., Zhao, H., Sanchez, W., Morgan, P.E., Greenleaf, J.F., Chen, S., . Application of attenuation measuring ultrasound shearwave elastography in 8 post-transplant liver patients, in: *2014 IEEE International Ultrasonics Symposium*, pp. 987–990.
- [25] Rau, R., Kruizinga, P., Mastik, F., Belau, M., de Jong, N., Bosch, J.G., Scheffer, W., Maret, G., a. 3d functional ultrasound imaging of pigeons. *NeuroImage* 183, 469–477.
- [26] Rau, R., Schweizer, D., Vishnevskiy, V., Goksel, O., b. Ultrasound aberration correction based on local speed-of-sound map estimation, in: *2019 IEEE International Ultrasonics Symposium (IUS)*, pp. 2003–2006.
- [27] Rau, R., Schweizer, D., Vishnevskiy, V., Goksel, O., 2019a. Speed-of-sound imaging using diverging waves.
- [28] Rau, R., Unal, O., Schweizer, D., Vishnevskiy, V., Goksel, O., 2019b. Attenuation imaging with pulse-echo ultrasound based on an acoustic reflector, in: *Medical Image Computing and Computer Assisted Intervention MICCAI 2019*, Springer International Publishing. pp. 601–609.
- [29] Sanabria, S., Martini, K., Freystätter, G., Ruby, L., Goksel, O., Frauenfelder, T., Rominger, M.B., 2019a. Speed of sound ultrasound: a novel technique to identify muscle loss in seniors. *European Radiology* 29, 3–12.
- [30] Sanabria, S.J., Goksel, O., 2016. Hand-held sound-speed imaging based on ultrasound reflector delineation, in: *MICCAI*, pp. 568–576.
- [31] Sanabria, S.J., Goksel, O., Martini, K., Forte, S., Frauenfelder, T., Kubik-Huch, R.A., Rominger, M.B., 2018a. Breast-density assessment with handheld ultrasound: A novel biomarker to assess breast cancer risk and to tailor screening? *European Radiology* 28, 3165–3175.
- [32] Sanabria, S.J., Ozkan, E., Rominger, M., Goksel, O., 2018b. Spatial domain reconstruction for imaging speed-of-sound with pulse-echo ultrasound: simulation and in vivo study. *Phys Med Biol* 63, 215015.
- [33] Sanabria, S.J., Rominger, M.B., Goksel, O., 2019b. Speed-of-sound imaging based on reflector delineation. *IEEE Trans Biomed Eng* 66, 1949–1962.
- [34] Sandrin, L., Tanter, M., Catheline, S., Fink, M., 2002. Shear modulus imaging with 2-D transient elastography. *IEEE Trans Ultras Ferr Freq Control* 49, 426–435.
- [35] Shanno, D., 1970. Conditioning of quasi-newton methods for function minimization. *Mathematics of Computation* 24, 647–656.
- [36] Smith, N.B., Webb, A.G., 2011. *Introduction to medical imaging: physics, engineering, and clinical applications*. Cambridge Univ. Press.
- [37] Treeby, B.E., Cox, B.T., 2010. k-Wave: MATLAB toolbox for the simulation and reconstruction of photoacoustic wave fields. *J Biomed Optics* 15, 021314.
- [38] Vishnevskiy, V., Rau, R., Goksel, O., 2019. Deep variational networks with exponential weighting for learning computed tomography, in: *Medical Image Computing and Computer Assisted Intervention MICCAI 2019*, Springer International Publishing. pp. 310–318.
- [39] Vishnevskiy, V., Sanabria, S.J., Goksel, O., 2018. Image reconstruction via variational network for real-time hand-held sound-speed imaging, in: *MICCAI Workshop on Machine Learning in Medical Image Reconstruction*, pp. 120–128.